The 2015-2016 Earthquake Sequence in Cushing, Oklahoma driven by Coulomb Stress Changes and Fluid Diffusions

Qingjun Meng [1], Sidao Ni [2], Zhigang Peng [3,*]

[1] Department of Geology and Geophysics, Texas A&M University, College Station, TX, USA (qimeng@tamu.edu)

[2] State Key Laboratory of Geodesy and Earth's Dynamics, Institute of Geodesy and Geophysics, Chinese Academy of Sciences,Wuhan, China (sdni@apm.ac.cn)

[3] School of Earth and Atmospheric Sciences, Georgia Institute of Technology, Atlanta, GA, USA (zpeng@gatech.edu)

Corresponding author: Zhigang Peng (zpeng@gatech.edu)

Key Points:

Slip distributions of the Cushing earthquake sequence are complex and complement with each other

Coulomb stress changes likely explain the space-time evolution of the Cushing earthquake sequence

Fluid diffusion also plays an important role in driving foreshock and aftershock migration

Abstract

An M5 earthquake occurred on November 7th, 2016, near the city of Cushing in Oklahoma, the largest crude oil storage site in the USA, after nearby disposal wells had been shut-in responding to three *M*4+ earthquakes in 2015. In this study, we investigated the rupture process of these *M*4+ events with finite fault model (FFM) inversions and computed Coulomb stress changes during this Cushing sequence. We found that the rupture processes of the four *M*4+ earthquakes are very complex, and they appeared to trigger one another, as evidenced by the inverted finite fault slip distribution and the calculated Coulomb stress change after each event. The foreshocks of the first M4 earthquake are probably triggered by Coulomb stress changes from previous earthquakes during 2014 and 2015 on unmapped faults several kilometers to the south. Fluid diffusion likely drives the bilateral seismic migration of the Cushing earthquake sequence after the foreshocks were triggered. In addition, fluid injection from the northwest of Cushing fault might have gradually increased the pore pressure on the Cushing fault, making the shallow part of the fault critically stressed.

Plain Language Summary

We studied the rupture process of four M4+ earthquakes and their foreshocks/aftershocks evolution process of the Cushing sequence, which occurred near the Cushing oil storage facilities and water disposal wells during 2015 and 2016. We found that the hypocenters of the four M4+ earthquakes occurred closely and their seismic slip patches complement each other in space on the unmapped Cushing fault. For the M4+ events, the stress status change caused by former

events contribute to triggering later event, implying a cascading trigger effect. Years before the Cushing sequence, the seismicity gradually migrated from several faults on south of Cushing fault until the foreshock sequence of Cushing sequence started, indicating foreshocks triggering effect. Both the foreshock triggering and the M4+ events triggering might be closely related with the water injection activity on northwest of Cushing city, because it might have increased the fluid pressure on the Cushing fault, making it a critically stressed fault susceptible for static stress triggering. The seismic bilateral expansions during the Cushing sequence also suggest a role by fluid diffusion. The seismic activity may be a composite product of both injection and tectonic stress transfer, that seismicity may start from areas far from the injection zone.

1. Introduction

Seismicity increased substantially in central United States beginning in 2008 (Ellsworth, 2013), and earthquakes in Oklahoma are the primary contributor of this surge (Keranen et al., 2014), with four *M* 5+ earthquakes occurred since 2011. Recent studies have shown that the sharp increase of seismicity and frequent occurrence of moderate-size events in Oklahoma are most likely linked with water disposal activity and hydraulic fracturing (e.g., Keranen et al., 2013; Yeck et al., 2017; Chen et al., 2017; Skoumal et al., 2019).

Several mechanisms have been proposed to explain the occurrence of induced earthquakes, including pore pressure increase resulted from fluid diffusion (Shapiro et al., 1997; Keranen et al., 2013; Chen et al., 2017), aseismic slip (Wei *et al.*, 2015), foreshock-induced Coulomb stress changes (Sumy *et al.*, 2014) and poro-elastically induced Coulomb stress changes (Segall and Lu, 2015; Goebel et al., 2017). In addition, recent studies attempted to examine other factors that govern locations and occurrence rates of induced earthquakes, such as injection volume and rates (Weingarten et al., 2015), injection depth to crystalline basement (Hincks et al., 2018), and competencies of rocks inferred from seismic tomography (Pei et al., 2018). However, it is still not clear which mechanisms or factors play the most important role in determining rate and maximum size of induced earthquakes (McGarr, 2017; Chen et al., 2018).

Most of these studies focus on examining seismicity and injection operations for the entire Oklahoma state or other regions. Only a few recent studies investigated an individual earthquake sequence or a small area in details (e.g., Goebel et al., 2017; Chen et al., 2018; Wu et al., 2019). As different faults might respond to fluid injection distinctively, it would be helpful to examine individual earthquake sequences to better understand the evolution of seismicity and mainshock source parameters, as well as the relationship with industrial water injection operation. These

results could be used, together with other recent studies, to provide useful information to operators and regulators in wastewater disposal regions to reduce potential impacts from induced earthquakes.

The M5 Cushing earthquake (November 7th, 2016, 01:44:24.500 UTC) is the latest *M* 5 event in Oklahoma (Figure 1). Similar to previous *M* 5 earthquakes in Oklahoma, it ruptured a previously unmapped fault (Yeck et al., 2017) about one mile to the west of Cushing city (Figure 1b). Cushing is a strategically important location with numerous intersecting pipelines and strategic storage facilities for crude oil in USA. Thus, the potential risk of damaging earthquakes in this region is much larger than in other regions in Oklahoma. While the M5 Cushing mainshock did not produce any damages to those storage facilities, some structural damages were found within the city (Taylor et al., 2017).

In October 2014, two M4+ earthquakes occurred along another unmapped fault just south of Cushing city (McNamara et al., 2015), raising the possibility of a large damaging earthquake along the Wilzetta-Whitetail fault zone further south of Cushing. One year before the 2016 Cushing *M* 5 earthquake, three *M* 4+ events occurred at nearly the same fault west of Cushing city (*Mwr*4.1, 09/18/2015 12:35:16.600 UTC; *M*wr 4.0, 09/25/2015 01:16:37.700 UTC; *Mwr* 4.3, 10/10/2015 22:03:05.300 UTC). After these *M* 4+events, Oklahoma Corporation Commission (OCC) required that injection wells within 3 miles from the earthquakes be shut in, and volume injected for wells within 6 miles should be reduced by 25 percent and wells from 6 to 10 miles may maintain the injection levels unincreased (OCC, 2015). However, a significant amount of waste water was then injected into a shallower formation (OCC). In November 2016, the *M* 5 event occurred nearly at the same locations of three M 4+ events.

Previous studies on M 5+ events in Oklahoma mostly involve teleseismic, InSAR or regional seismic data to invert for the slip models (Sun et al., 2014; Grandin et al., 2017). The Cushing earthquake sequence (three *M* 4+ and one M5 event) is relatively small in magnitude, with the largest mainshock only about M 5. Hence, teleseismic and InSAR data do not provide the highest resolution to reveal detailed rupture processes. Recently, based on local broadband recordings, Wu et al. (2019) utilized a time domain empirical Green's function (EGF) deconvolution method to retrieve relative source time functions (RSTFs) of the 2015 M4.0 Guthrie earthquake, and found four sub-events propagating unilaterally to the southwest. Their study highlighted the importance of local waveform recordings for high-resolution source imaging of moderate-size events.

For the 2015-2016 Cushing sequence, several nearby seismic stations (with both broadband and strong motion sensors) are available, including three seismometers within 5 km and the closest station less than 2 km from the 2016 M5 mainshock, providing an excellent opportunity to reveal fine details of their rupture processes. Combining with precise microseismicity relocation results and comparing with the water injection data, we can better understand the spatio-temporal evolution and triggering behavior of this earthquake sequence.

2. Spatio-Temporal Evolutions of Seismicity

Based on catalogs and phase arrivals from National Earthquake Information Center (NEIC) and Oklahoma Geological Survey (OGS), Schoenball and Ellsworth (2017a) used HYPOINVERSE-2000 (Klein, 2014) and hypoDD packages (Waldhauser and Ellsworth, 2000) to relocate earthquakes in Oklahoma and southern Kansas from May 2013 to November 2016 (Figure 1a-d). From their relocation result (Figure 1), the 2015-2016 Cushing seismic sequence occurred along a narrow zone along profile AA' striking 60° clockwise from north, with a nearly vertical fault

geometry (hereafter termed the Cushing Fault). This is consistent with the right-lateral strike-slip focal mechanisms with steep dip angles (Figure 1b and Table 1) from our point-source focal mechanism inversion results for four events in this sequence (next section). From the relocation result along profile AA', we found that four *M*4-5 events and their aftershocks occurred at shallow depth between 2 to 5 km.

Next we examined the seismicity pattern in a longer time window (2013-2020). Because the relocated catalog of Schoenball and Ellsworth (2017a) is between 2013 and 2016, we used both the relocated (Figure 2) and the standard (Figure S1) OGS catalogs (Walter et al., 2019). In addition, we compared with a relocated catalog (Figure S2) based on template matching (Skoumal et al., 2019). Generally, the seismic evolution history near Cushing city could be summarized by four main stages: I, II, III and IV. In stage I, the seismicity rate was low in 2013 but surged since 2014, concentrating along a short WNW unmapped fault (CC' in Figure 2) on the south of the Cushing fault (AA' in Figure 2a). The increased seismicity includes two left-lateral strike slip *M* 4 earthquakes on October 2014 (Figure 2a), implying a left-lateral strike-slip nature of fault CC' (McNamara et al., 2015). In stage II, between October 2014 to September 18, 2015, a seismic swarm began to concentrate along a ~60 degree striking short fault (marked as DD’ in Figure 2b) to the northwest of the two M4 earthquakes. By checking the first motions of four M>3 earthquakes within this warm, it seems that all of them are consistent with right-lateral strike slip focal mechanisms (Figure S3) and the largest event is of magnitude 3.4 on 09/01/2015.

At the end of stage II (09/15/2015), three days before the first M 4.1 earthquake on 09/18/2015, seismicity started occurring on the western part of the ENE-striking Cushing fault (AA' in Figure 2b), followed by three *M* 4+ earthquakes together with their aftershocks along this right-lateral fault (Figure 2c) a few days later in stage III. The seismicity started at around 3

km along the AA’ projection staring at 09/15/2015 and showed bi-lateral expansion along both directions (Figure 2h). Such expansion is also clear in the original OGS catalog (Figure S1) and the template-matching catalog (Figure S2). Because the seismic activity increased steadily without a mainshock, this sequence can be classified as earthquake swarms (e.g., Mogi, 1990). For the sake of discussion later, we also termed the seismicity before the first M 4.1 event on 09/18/2015 as foreshocks. In stage III, after the three M 4+ earthquakes occurred along fault AA’, many earthquakes occurred surrounding the Cushing city. Earthquakes started to occur at the eastern end of fault CC' from March to May in 2016 and seismicity started to occur to the north of fault AA’ from June to November 2016. In stage IV, following the *M* 5 event on Nov. 7, 2016, nearly all seismicity concentrated along the fault AA' for about 9 kms. The seismic activity on adjacent faults was suppressed since then and the Cushing fault AA' became dominant without significant seismic activity around Cushing area up to 2020 (Figure S1).

3. Path Calibration for Source Inversion

Because *M*4+ events are relatively small, detailed analysis of their rupture process requires modeling of high-frequency seismic waveforms. To ensure that propagation effects are properly modeled at high frequencies, we refined the 1D velocity structure and performed path calibration using four *M*3+ reference events (Table S1) located along the ruptured fault (Figure 1c-d). For these reference *M*3+ events, their corner frequencies are higher and source time functions are relatively simpler than the targeted *M*4-5 events, which could be approximated as point sources. In addition, the four reference events occurred after Nov. 9, 2016, when two close-by seismic stations (OK052 and OK053) were deployed, thus providing valuable data for reliable waveform modeling. Together with other nearby stations (Figure 1), we used hypo2000 method (Klein,

2014) to gain more precise relocation for these reference events, which improve the path calibration by minimizing the location uncertainty.

To obtain a refined velocity structure (Figure 3), we first fixed the basement depth at about 2.0 km, which was referred from Keranen et al. (2013) and based on the completion depths of nearby injection wells. We grid searched for an optimal Vp of the top rock layer and the optimal depth of Vp equals to 4.0 km/s, D_vp4 (Wei et al, 2015). An empirical relationship of Vs = (Vp − 1.36)/1.16 was used to estimate Vs from Vp within each layer (Brocher, 2005). In addition, considering the effects of unconsolidated sediments in the near surface, a thin (8 m thick) low-velocity layer was added as the top layer, with Vp= 1.7 km/s and Vs=0.3 km/s (Taylor et al., 2017). Within each tested velocity model, we calculated synthetic waveforms of four reference events based on Green's functions computed with a frequency-wavenumber integral algorithm (Zhu and Rivera, 2002) and a uniform focal mechanism of strike/dip/rake of 60°/90°/0°. These numbers are based on the focal mechanisms of the *M*4-5 earthquakes (Table 1) and the spatial distribution of their aftershocks (Figure 1). To avoid the influence of depth uncertainty from reference events, the focal depth was slightly adjusted around the relocated depth to achieve the best match between the observation and synthetics. Using the optimal refined velocity model VM3 (Table S2), the average correlation-coefficient (CC) between the observed three-component waveforms and the synthetics reaches to the highest value of about 0.54 (Figure S4). In comparison, The Keranen et al. (2013) model VM2 yields an average CC of about 0.38, and the Crust2.0 model (Bassin *et al.*, 2000) VM1 results in an average CC lower than 0.1.

4. Finite Fault Model and Stress Drop Estimate

From the raw seismic waveforms, the *M* 5 mainshock appeared to have two sub-events, and the differential S wave arrival times for two sub-events can be seen clearly on four close seismic

stations (Figure 4b). By matching the observed and synthetic S waves arrival time difference, we grid-searched the initiation point and origin time of the second sub-event (Figure 4a). Although the depth constraint is relatively poor compared with the horizontal constraint, the second sub-event is found to initiate about 3 km to the north of the first sub-event along the fault, and about 1 s later after the first sub-event. This suggests a rupture speed of at least 3 km/s for the M 5 mainshock. From the raw seismic data of three M4+ events (Figure 4c), we found that the S waves are also very complex, not as simple and clean as the reference events (Figure S4). This implies that all events in Cushing earthquake sequence involve complicated rupture processes, which could be revealed from the finite fault inversion results below.

With the optimal velocity structure, we inverted for the rupture process of *M*4-5 Cushing earthquakes and calculated their stress drops. We used three-component waveform data from seismic stations within epicentral distance of 15 km, and band-pass filtered velocity waveforms from 0.2 to 3 Hz. Rupture initiation points (i.e., hypocenters) are based on the relocated catalog (Schoenball and Ellsworth, 2017a) and the geometries of fault models are based on focal mechanisms inverted by the Cut and Pasted (CAP) method (Zhu et al., 2013). Then we performed an inversion of finite fault model (FFM) for each event (Hartzell and Heaton, 1983; Yue and Lay, 2013), with the fault model consisting of 77 grids with each cell size of 0.5×0.5 km, and the total fault dimensions of 6.5×6.5 km. The source time function (STF) of each grid is parameterized as 6 symmetric triangles of 0.15 s rise time with an offset of 0.15 s each. During the FFM inversion process, the rupture speed for the M 5 mainshock is set at 3 km/s (as inferred from the direct waveform observation in Figure 4a). The rupture speed for three M 4+ events is set as 2.5 km/s, which is about 75% of S wave velocity and could fit the observed waves well. The smoothing factors are set as 3.5×10^{-5}, after comparing the waveforms fitting misfit under a

series of smoothing factor values (Figure S5) and examining the check-board recovery result (Figure S6).

The inverted slip models, waveform fittings and STFs for the four earthquakes are shown in Figures 5 and 6. Although three *M* 4+ events are relatively small in magnitude, their slip patterns are more complex than expected, with each event involving several slip patches. As mentioned above, the *M* 5 earthquake slipped on two relatively discrete areas, with the inverted maximum slip around 15 cm and the final moment magnitude of *Mw* 4.9 (Figure 5d). After it ruptured for the first 0.5 -1 s, the rupture slowed down and paused for around 0.5 s before further propagation along the NE side of the Cushing fault (Figure 5d and 6d). Comparing the slip contours of four M4+ earthquakes (Figure 5e), their slip patches seem to partially complement with each other, with minor overlap. The hypocenter of the Mw 4.9 event is surrounded by the slip patches of three former M4+ events.

With the inverted slip models, we computed Coulomb stress changes on the right-lateral strike-slip fault for four earthquakes, using the Coulomb3 software (Toda et al., 2011). Similar to previous studies (Stein et al., 1992; Toda et al., 2011), we used an effective coefficient of friction of 0.4. We summed the Coulomb stress change for each main event, assuming that any succeeding earthquake is affected by the cumulative stress changes caused by previous earthquakes. For example, the 10/10/2015 Mw 4.3 event could be affected by the cumulative Coulomb stress change from 09/28/2015 Mw 4.1 and 09/25/2015 Mw 4.0 event. As shown in Figure 7, we found that most of aftershocks and subsequent M 4+ earthquake occurred near the boundary between the stress drop and stress increase areas. Although some uncertainties of seismicity relocations and finite fault slip inversion may still remain, it suggests that Coulomb

stress changes from previous earthquakes played an important role in triggering subsequent earthquakes.

The obtained maximum stress drops for these four events are: 0.6, 1, 2 and 8 MPa, respectively and the average stress drops are even lower. They are relatively low compared with the average value of 14 MPa (Atkinson and Boore, 2006) or 18-25 MPa (Boore et al., 2010) for central and eastern North American earthquakes. On the other hand, these stress drops are comparable with the values from injection-induced earthquakes in other regions. For example, Justinic et al. (2013) obtained an average stress drop of about 4.3 MPa for seven injection-induced earthquakes in Cleburne, Texas. Wu et al. (2018) also found an average stress drop of 2.0 MPa for induced earthquakes in Oklahoma. However, with the same spectral ratio methods, Huang et al. (2017) found that induced earthquakes have a comparable median stress drop to shallow tectonic earthquakes in the central United States. Similarly, Daniels et al. (2020) used the special ratio method and found that the 2014/02/15 M4.1 South Carolina earthquake and its M3.0 aftershock (most likely natural events) had stress drop values of 3.75 and 4.44 MPa, respectively. They argued that most injection-induced earthquakes (and the 2014 South Carolina earthquake) were shallow (~3-5 km depth), and shallow earthquakes generally have lower stress drops than earthquakes at larger depth (Shearer et al., 2006).

5. Water Disposal and Stress Transfer

The Arbuckle group is the deepest sedimentary layer overlying the crystalline basement throughout Oklahoma (Murray et al., 2014). Hence, it is a favorable formation for wastewater disposal. Near Cushing, all disposal wells within 10 miles from hypocenters of four *M*4-5 events inject wastewater into the Arbuckle group at ~1.2–2.0 km at depth. This is supported by

checking the minimum and maximum depth of well completions (Figure 8b). The closest four injection wells, within 3 miles, are all located to the north and west of four M4-5 epicenters (Figure 1b). Analysis of OCC's monthly injection rate for the disposal wells within epicentral distance of 3, 6 and 10 miles (Figure 1a), shows that injection rate increased gradually since 2011 and remained at a high level from January 2014 to September 2015 (Figure 8a). Most of the injection data in 2013 is missing, due to the lost contact with an operation company that went bankrupted in 2013 (private communication with OCC, 02/2019). The monthly injection into Arbuckle group reduced twice, in 2015 after the three M4+ events and in 2016 after the M 5 event. The Arbuckle injection of four closest wells, within 3 miles, dropped to zero since October 2015. However, a large amount of water started to be injected into a shallower formation after October 2015, for all injection wells within epicentral distance of 10 miles.

At present, without a good estimation of the permeability for the Arbuckle group, other shallow formations, the basement and active fault zones, it is challenging to perform a realistic simulation for water diffusion process or calculate the pore pressure and stress perturbation due to fluid injection. Hence, it would be difficult to examine the causal relationship between the seismic activity and water diffusion effect. Generally, water diffusion from nearby injection wells since 2011 could gradually increase the pore pressure and reduce the fault strength on the Cushing fault, leading to a critically stressed fault with increased seismic activity. We analyzed the variance of seismicity rate from 2011 to 2020, within epicentral distance of 10 miles and the magnitude completeness Mc is M 2.3 (Figure S7). The seismicity rate surged since 2014, consistent with the increased water injection rate after 2014 (Figure 8a). As mentioned before, an injection reduction operation was imposed by OCC since October 2015, immediately after three *M* 4+ events occurred. In addition, after the M 5 event in November 2016, the Arbuckle injection

dropped to a very low level. The average seismic rate was lower since then, consistent with the reduction of injection operation.

Foreshocks of the Cushing sequence started from 09/15/2015, three days before the 09/18/2015 M4.1 event, and in the following one month seismicity showed a bilateral migration pattern along fault AA'(e.g., Figure 2h). We plotted the expected fluid diffusion curves with the following equation: $r = \sqrt{4\pi Dt}$, where r is distance to the starting point of seismicity along AA' and t is the time lapse. The seismicity in the foreshock sequence (i.e., from 09/15/2015 to before the 09/18/2015 M4.1 event) expanded rapidly along the strike at the beginning, which might be related with the Coulomb stress triggering to be discussed later. Hence, we set the migration starting point of seismicity at point O and P along fault AA' on 09/15/2015 (Figure 2h). The seismicity migrated from O towards A direction and migrated from P towards A' direction on the other side. As shown in Figure 2h, the corresponding D values range from 0.05 to 0.1 m^2/s from the relocated catalog of Schoenball and Ellsworth (2017a). If we use the OGS (Walter et al.,2019) and the template matching (Skoumal et al., 2019) catalogs, the corresponding D values are in the range of 0.05–0.1 m^2/s (Figure S1) and 0.12–0.22 m^2/s (Figure S2), respectively. These numbers are roughly within the range of estimations for the entire Oklahoma and Southern Kansas (Schoenball and Ellsworth, 2017b), and smaller than those in volcanic regions (Shelly et al., 2013a, 2013b). Such a rapid expansion of seismicity generally suggests a triggering by fluid pressure diffusion (Shapiro et al., 1997; Hainzl, 2004). However, the seismic migration might be related with bilateral aseismic slip after each M 4+ event, whose effect is difficult to be evaluated without geodetic data.

After we analyzed the evolution of seismicity along fault CC', DD' and AA', we calculated the Coulomb stress changes caused by several sequences (Figure 9), using an effective friction

coefficient μ’ = 0.4. The Coulomb stress changes are resolved on the right-lateral fault striking 360 degrees at depth of 3 km, using the centroid location and mechanism information of the two M4 earthquakes on fault CC’ (2014) from McNamara et al. (2015). We found that the seismic swarm during 2014 and 2015 (marked as DD’ in Figure 2b) to the northwest of the two M4 events is located within the Coulomb stress increase area (Figure 9c), indicating that they were likely triggered by static stress change after two M4 earthquakes. This inference is also consistent with their right-lateral focal mechanisms (Figure S3). The western end of the Cushing fault AA’ is also within the Coulomb stress increase area. We also calculated the Coulomb stress change caused by the seismic swarm (the largest event has a magnitude 3.4) and found that it causes a subtle stress increase (~2-5 kPa) on the Cushing fault (Figure 9e-f), especially covered the zone of four hypocenters of the Cushing earthquake sequence. The cumulative Coulomb stress change on the Cushing fault, as shown by the map view and depth section in Figure 9d-e, illustrates that the foreshocks of the 2015-2016 Cushing sequence (i.e., between 09/15/2015 and 09/18/2015) are located close to the boundary of stress increase and stress drop areas. If we used smaller effective friction coefficient μ’, for example 0.1 (Figure S8), all foreshocks and the hypocenters of Cushing earthquake sequence fell within the Coulomb stress increase area. This is because with a near zero μ’, the Coulomb stress on fault AA’ is less affected by the normal stresses and mostly affected by the shear stress (Figure 9a-b). Hence, the resulting Coulomb stress increase zone is shifted slightly towards the eastern side along fault AA’. On the other hand, if a higher effective friction coefficient is used, for example 0.68 (Figure S9) as used in Qin et al. (2018), the Coulomb stress increase area is shifted to the western side along fault AA’ and most of foreshocks and M4+ hypocenters are included in the Coulomb stress decrease area (i.e., stress shadow). In fluid injection regions in Oklahoma, we expect presence of high fluid

pressures, which would result in low effective friction coefficient μ'. Hence, we argue that a relatively small value μ' should be used, which would also favor the interpretation that the 2015-2016 Cushing sequence was likely triggered by Coulomb stress changes from sequences a few kilometers in the south.

6. Discussion

The evolution of seismicity is rather complicated, which migrated from an unmapped fault (CC') in the south to a nearby unmapped fault (DD'), and then to the AA' Cushing fault on the north. Such evolution can be qualitatively explained by the static Coulomb stress transfer. Because the Coulomb stress change is on the order of a few KPa, we argue that the areas around the hypocenters of the Cushing sequence are already critically stressed. In addition, the stress transfer originates from the fault further away from water injection wells towards the fault close to the injections well, instead of the opposite direction. When the foreshock sequence started 3 days before the first M4.1 event, the seismicity front expands outward with time following $\sqrt{t}$, consistent with being driven by fluid diffusion (Shapiro *et al*., 1997; Hainzl, 2004). In addition, our finite-fault inversion results suggest that the slip regions of four M4+ events mostly complemented with each other, and the next event generally started at the edge of the previously ruptured region. Putting together, these results suggest a combined effects of Coulomb stress changes at different space-time scales, combined with fluid diffusions in driving the entire Cushing earthquake sequences.

McGarr et al. (2017) suggested the possibility of another M > 5 earthquakes to occur near Cushing city in the future, based on the large amount of total injection volume. By analyzing the seismicity pattern, we found that seismicity remains active along fault AA' after the M 5

mainshock, as evidenced by several small earthquake swarms occurred in 2016, 2017 and 2019, near the hypocenter of M 5 mainshock (Figure S1g). In addition, our Coulomb stress calculations suggested that a region to the SW side and the central part (Figure 7d) of the Cushing fault are positively stressed, and did not rupture during the recent sequence. So it is likely a possible source region for future earthquakes. However, the overall injection volume and the seismicity rate were steadily decreasing since 2016 (Figure 8). Hence, we argue that the seismic risk around Cushing could be relatively reduced as compared with before, unless large stress is transferred from the surrounding faults. Of course, our argument might be flawed since we did not consider other unmapped faults (e.g., DD' in Figure 2) that are closer to the city.

In this study, the earthquake locations and finite fault inversion of *M* 4+ events are possible due to the availability of waveform data from a few seismometers very close the fault. In the near future, dense seismic arrays near water disposal wells are essential for detecting weak seismic events and studying rupture characteristics of induced earthquakes. In addition, water diffusion and earthquake rupture simulation could be implemented with more realistic multiple fault system and material properties, in order to better understand the relationship between fluid injection and evolution of seismicity. These are beyond the scope of this study and will be pursued in subsequent work.

7. Conclusion

In this study, we analyzed the rupture process of four *M*4-5 earthquakes, spatio-temporal evolution of seismicity, water disposal history near Cushing city and stress transfer process during the Cushing sequence. We found that the hypocenters of Cushing four earthquakes are

very close and their inverted slip patches generally complement each other along fault AA'. Each M 4+ earthquake in Cushing earthquake sequence was located on the boundary of Coulomb stress change areas, implying a cascade Coulomb stress triggering effect. The 11/07/2016 *Mw* 4.9 mainshock could be triggered by the cumulative Coulomb stress increase caused by three previous M 4+ earthquakes from September and October 2015, though the mainshock occurred one year later after the three M 4+ earthquakes. Before the Cushing earthquake sequence, the seismicity migrated from unmapped faults CC' to DD' and then to the Cushing fault AA'. The foreshock sequence of Cushing earthquake sequence starting three days before the first M4 earthquake, and occurred in the Coulomb stress increase region. The water injection activity on northwest of Cushing increased the fluid pressure on the Cushing fault, making it a critically stressed fault more susceptible for static stress triggering by seismic activities along the upmapped faults CC' and DD'. The seismic bilateral expansions during the Cushing earthquake sequence also suggest a role by fluid diffusion. While the southwestern and central part of the Cushing fault are in the zones with positive Coulomb stress changes and remain un-ruptured, the overall injection volume and background seismicity around Cushing have reduced since 2016. Hence, the seismic risk around Cushing is further reduced as compared with before.

Acknowledgement and Data

The seismic waveform data are downloaded from IRIS Data Management Center (http://ds.iris.edu/wilber3/find_event). Earthquake catalog in this study is from National Earthquake Information Center (https://earthquake.usgs.gov/earthquakes/search/) and Oklahoma Geological Survey (OGS, https://ogsweb.ou.edu/eq_catalog/). Fault plane solutions are obtained from OGS. Information on well completions and monthly injection data are downloaded from

Oklahoma Corporation Commission (http://www.occeweb.com/og/ogdatafiles2.htm). Some figures are made using Generic Mapping Tools (www.soest.hawaii.edu/gmt, last accessed January 2017; Wessel and Smith 1998). This research is supported by National Natural Science Foundation of China (Grant Number: 41304040) and US National Science Foundation (Grant Number: 1818611). Thanks for inspiring discussion with Dawid Szafranski and Benchun Duan, from Texas A&M University, about water diffusion. This manuscript benefits from useful comments by Xiaowei Chen from University of Oklahoma and Xiaofeng Meng from University of Southern California.

Reference:

Atkinson G. M., and Boore D. M., 2006. Earthquake ground-motion prediction equations for eastern North America, *Bull. Seismol. Soc. Am.*, 96, 2181–2205, doi:10.1785/0120050245.

Bassin, C., G. Laske, and G. Masters, 2000. The current limits of resolution for surface wave tomography in North America, *Eos Trans. AGU*, **81**(48), Fall Meet. Suppl., Abstract S12A–03.

Boore D. M., Campbell K. W., and Atkinson G. M., 2010. Determination of stress parameters for eight well-recorded earthquakes in eastern North America, *Bull. Seismol. Soc. Am.*, 100, 1632–1645, doi:10.1785/0120090328.

Brocher, T.A., 2005. Empirical relations between elastic wavespeeds and density in the Earth's crust. Bull. Seismol. Soc. Am.95, 2081–2092. http://dx.doi.org/10.1785/0120050077.

Chen X. et al., 2017. The Pawnee earthquake as a result of the interplay among injection, faults and foreshocks, *Scientific Reports*, 7:4945, DOI:10.1038/s41598-017-04992-z.

Chen, X., Haffener, J., Goebel, T. H. W., Meng, X., Peng, Z., and Chang, J.C., 2018. Temporal correlation between seismic moment and injection volume for an inducedearthquake sequence in central Oklahoma. *Journal of Geophysical Research: Solid Earth*, *123*, 3047–3064.https://doi.org/10.1002/2017JB014694.

Daniels, C., Z. Peng, Q. Wu, S. Ni, X. Meng, D. Yao, L. S. Wagner, and K. M. Fischer, 2020. The 15 February 2014 Mw 4.1 South Carolina Earthquake Sequence: Aftershock Productivity, Hypocentral Depths, and Stress Drops, Seismol. Res. Lett. 91, 452–464, doi: 10.1785/0220190034.

Ellsworth W. L., 2013. Injection Induced earthquakes, Science 341, 1225942. DOI: 10.1126/science.1225942

Goebel, T. H. W., Weingarten, M., Chen, X., Haffener, J., and Brodsky, E. E., 2017. The 2016 Mw5.1 Fairview, Oklahoma earthquakes: Evidence for long-range poroelastic trigerring at >40 km from fluid disposal wells. *Earth and Planetary Science Letters*, 472, 50–61. https://doi.org/10.1016/j.epsl.2017.05.011.

Grandin R, Vallée M, Lacassin R., 2017. Rupture Process of the *Mw* 5.7 Pawnee, Oklahoma, Earthquake from Sentinel-1 InSAR and Seismological Data[J]. *Seismol. Res. Lett.*,*88*

Hartzell, S. H., and T. H. Heaton, 1983. Inversion of strong ground motion and teleseismic waveform data for the fault rupture history of the 1979 Imperial Valley, California, earthquake, Bull. Seismol. Soc. Am., 73(6A), 1553–1583.

Hainzl, S., 2004. Seismicity patterns of earthquake swarms due to fluid intrusion and stress triggering, Geophys. J. Int., 159, 1090–1096.

Hincks T. , Aspinall W. , Cooke R. , Gernon T., 2018. Oklahoma's induced seismicity strongly linked to wastewater injection depth, Science, 359(6381), 1251–1255, doi.org/10.1126/science.aap7911.

Huang, Y., Ellsworth, W. L., & Beroza, G. C., 2017. Stress drops of induced and tectonic earthquakes in the Central United States are indistinguishable. *Science Advances*, **3**(8), e1700772. https://doi.org/10.1126/sciadv.1700772.

Justinic A. H., Stump B., Hayward C., and Frohlich C., 2013. Analysis of the Cleburne, Texas, earthquake sequence from June 2009 to June 2010, Bull. Seismol. Soc. Am., 103(6), 3083–3093, doi:10.1785/0120120336.

Keranen, K., H. M. Savage, G. Abers, and E. S. Cochran, 2013. Potentially induced earthquakes in Oklahoma, USA: Links between wastewater injection and the 2011 M_W 5.7 earthquake sequence, *Geology*, 41, 699–702, doi:10.1130/G34045.1.

Keranen, K. M., M. Weingarten, G. A. Abers, B. A. Bekins, and S. Ge, 2014. Induced earthquakes. Sharp increase in central Oklahoma seismicity since 2008 induced by massive wastewater injection, *Science,345(6195)*, 448–51.

Klein, F. W., 2014. User’s guide to HYPOINVERSE-2000, a Fortran program to solve for earthquake locations and magnitude, U.S. Geol. Surv. Open-File Rept. 02-171, revised June 2014.

Marsh, S., Holland A., 2016. Comprehensive Fault Database and Interpretive Fault Map of Oklahoma, OF2-2016.

McGarr, A., & Barbour, A. J., 2017. Wastewater disposal and the earthquake sequences during 2016 near Fairview, Pawnee, and Cushing, Oklahoma. Geophysical Research Letters, 44, 9330–9336. https://doi.org/10.1002/2017GL075258.

McNamara, D. E., et al., 2015. Reactivated faulting near Cushing, Oklahoma: Increased potential for a triggered earthquake in an area of United States strategic infrastructure, *Geophys. Res. Lett.*, 42, 8328–8332, doi:10.1002/2015GL064669.

Murray, K. E., 2014. Class II Underground Injection Control Well Data for 2010–2013 by Geologic Zones of Completion. Oklahoma Geological Survey Open File Report OF1-2014, 32.

Mogi, K., H. Mochizuki, and Y. Kurokawa, 1990. Changes in hot springs in the Usami-Ito area related to the 1989 Ito-oki earthquake swarm and submarine eruption, Rep. Coord. Comm. Earthq. Predict., 43, 290-299.

Oklahoma Corporation Commission, 2015. Media advisory—Cushing earthquakes. [Available at http://www.occeweb.com/News/10-19-15CUSHING 2.pdf.]

Pei, S., Peng, Z., and Chen, X., 2018. Locations of injection-induced earthquakes in Oklahoma controlled by crustal structures. *J. Geophys. Res. Solid Earth*, 123, 2332–2344, doi.org/10.1002/2017JB014983.

Qin, Y., Chen, X., Carpenter, B. M., & Kolawole, F., 2018. Coulomb stress transfer influences fault reactivation in areas of wastewater injection. Geophysical Research Letters, 45, 11,059–11,067.

Schoenball, M., & Ellsworth, W., 2017a. Waveform relocated earthquake catalog for Oklahoma and Southern Kansas illuminates the regional fault network. *Seismological Research Letters*, 88(5), 1252–1258. https://doi.org/10. 1785/0220170083.

Schoenball, M., & Ellsworth, 2017b. W., A systematic assessment of the spatiotemporal evolution of fault activation through induced seismicity in Oklahoma and southern Kansas. Journal of Geophysical Research: Solid Earth, 122, 10,189–10,206. https://doi.org/10.1002/2017JB014850.

Segall P., and Lu S., 2015. Injection-induced seismicity: Poroelastic and earthquake nucleation effects, *J. Geophys. Res. Solid Earth*, 120, 5082–5103, doi:10.1002/2015JB012060.

Shapiro, S. A., E. Huenges, and G. Borm, 1997. Estimating the crust permeability from fluid-injection-induced seismic emission at the KTB site, Geophys. J. Int., 131, F15–F18.

Shearer, P. M., G. A. Prieto, and E. Hauksson, 2006. Comprehensive analysis of earthquake source spectra in southern California, J. Geophys. Res., 111, B06303, doi:10.1029/2005JB003979.

Shelly, D. R., S. C. Moran, and W. A. Thelen, 2013a. Evidence for fluid-triggered slip in the 2009 Mount Rainier, Washington earthquake swarm, Geophys. Res. Lett., 40, 1506–1512, doi:10.1002/grl50354.

Shelly, D. R., D. P. Hill, F. Massin, J. Farrell, R. B. Smith, and T. Taira, 2013b. A fluid-driven earthquake swarm on the margin of the Yellowstone caldera, J. Geophys. Res. Solid Earth, 118, 4872–4886, doi:10.1002/jgrb.50362.

Skoumal, R. J., Kaven, J. O., & Walter, J. I., 2019. Characterizing seismogenic fault structures in Oklahoma using a relocated template-matched catalog. Seismological Research Letters, 90(4), 1535–1543. https://doi.org/10.1785/0220190045.

Stein, R. S., G. C. P. King, and J. Lin, 1992. Change in failure stress on the southern San Andreas fault system caused by the 1992 magnitude = 7.4 Landers earthquake, Science, 258, 1328–1332.

Sumy, D. F., Cochran E. S., Keranen K. M., Wei M., and Abers G., 2014. Observations of static Coulomb stress triggering of the November 2011 M 5.7 Oklahoma earthquake sequence, *J. Geophys. Res. Solid Earth*, 119, 1904–1923, doi:10.1002/2013JB010612.

Sun X., and Hartzell S., 2014. Finite- fault slip model of the 2011 Mw 5.6 Prague, Oklahoma earthquake from regional waveforms, *Geophys. Res. Lett.*, 40, 4207–4213, doi:10.1002/2014GL060410.

Talwani, P., Chen, L. & Gahalaut, K, 2007. Seismogenic permeability, ks. Journal of Geophysical Research: Solid Earth 112, 1–18.

Taylor J. et al., 2017. M5.0 Cushing, Oklahoma, USA Earthquake on Noverber 7, 2016, EERI Earthquake Reconnaissance Team Report.

Toda, S., R. S. Stein, V. Sevilgen, and J. Lin, 2011. Coulomb 3.3 Graphic-Rich Deformation and Stress-Change Software for Earthquake, Tectonic, and Volcano Research and Teaching – User Guide, *U. S. Geol. Surv. Open-File Rep. 2011-1060*.

Waldhauser, F., and W. L. Ellsworth, 2000. A double-difference earthquake location algorithm: Method and application to the northern Hayward fault, California, Bull. Seismol. Soc. Am. 90, no. 6, 1353–1368, doi: 10.1785/0120000006.

Walter, J. I., P. Ogwari, A. Thiel, F. Ferrer, I. Woelfel, J. C. Chang, A. P. Darold, and A. A. Holland, 2019. The Oklahoma Geological Survey Statewide Seismic Network, Seismol. Res. Lett. 91, 611–621, doi: 10.1785/0220190211.

Wei, S. *et al.*, 2015. The 2012 Brawley swarm triggered by injection-induced aseismic slip, *Earth and Planetary Science Letters* 422, 115-125.

Weingarten, M., S. Ge, J. W. Godt, B. A. Bekins, and J. L. Rubinstein, 2015. High-rate injection is associated with the increase in U.S. mid-continent seismicity, *Science*, 348(6241), 1336–1340, doi:10.1126/science.aab1345.

Wu, Q., Chapman, M. C., & Chen, X., 2018. Stress-drop variations of induced earthquakes in Oklahoma. *Bulletin of the Seismological Society of America*, **108**(3A), 1107–1123. https://doi.org/10.1785/0120170335.

Wu, Q., Chen, X., & Abercrombie, R. E., 2019. Source complexity of the 2015Mw 4.0 Guthrie, Oklahoma earthquake. Geophysical Research Letters, 46, 4674–4684. https://doi.org/10.1029/2019GL082690.

Yeck, W. L., G. P. Hayes, D. E. McNamara, J. L. Rubinstein, W. D. Barnhart, P. S. Earle, and H. M. Benz, 2017. Oklahoma experiences largest earthquake during ongoing regional wastewater injection hazard mitigation efforts, *Geophys. Res. Lett.*,*44*, 711–717.

Yue, H., and T. Lay, 2013. Source rupture models for the Mw 9.0 2011 Tohoku earthquake from joint inversions of high-rate geodetic and seismic data, Bull. Seismol. Soc. Am., 103, 1242–1255, doi:10.1785/0120120119.

Zhu L. and Ben-Zion Y., 2013. Parameterization of general seismic potency and moment tensors for source inversion of seismic waveform data, *Geophys. J. Int*., 194, 839-843

Zhu, L., and L. Rivera, 2002. A note on the dynamic and static displacements from a point source in multilayered media, *Geophys. J. Int.*, **148(3)**, 619– 627.

Figures and Tables:

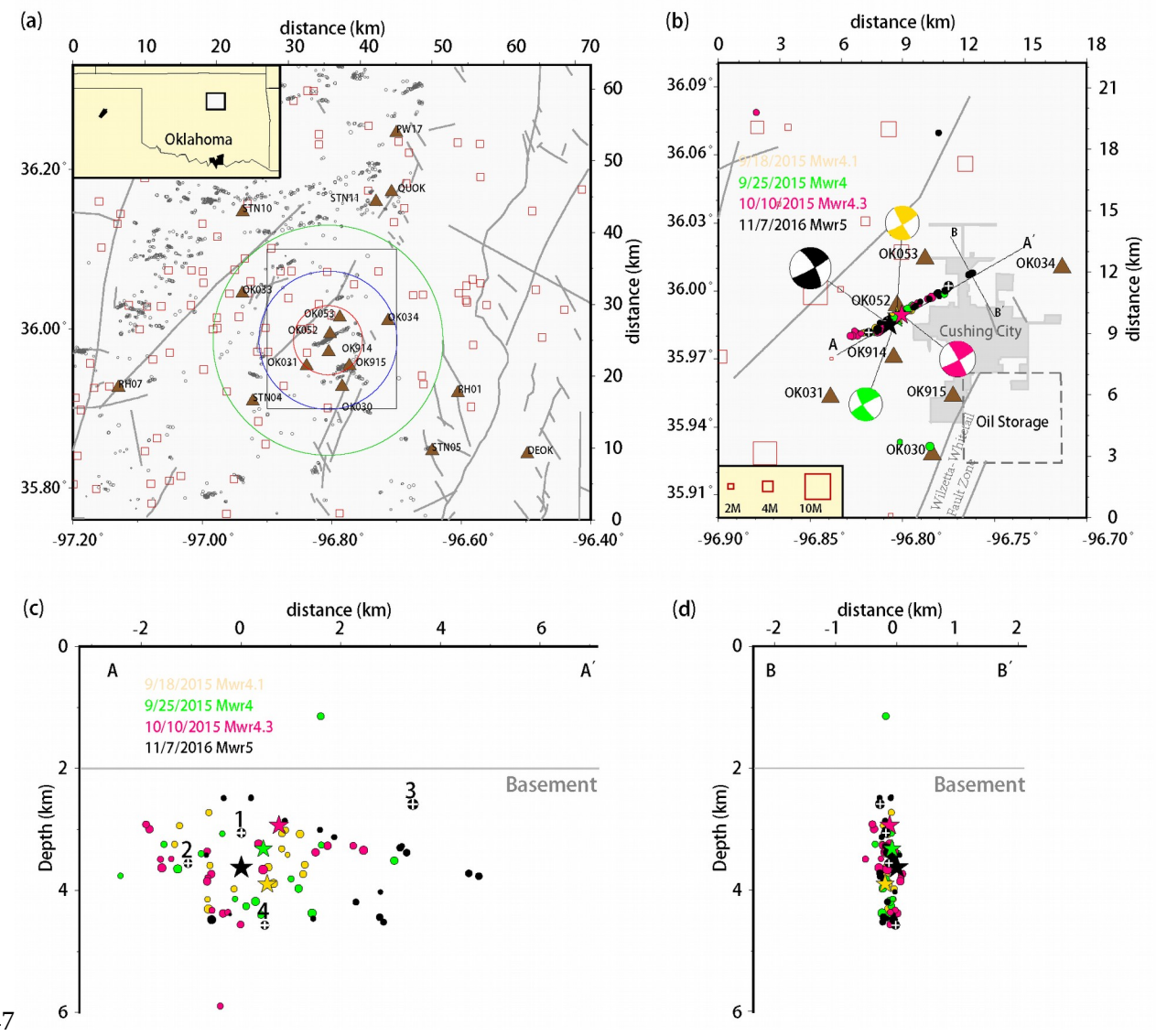

Figure 1. Seismicity near Cushing city, and seismic stations and disposal wells. (a) Seismicity (grey circles) from May 2013 to November 2016 using the catalog from Schoenball and Ellsworth (2017a). Disposal wells are indicated with red squares. Browns triangles show seismic stations within 35km epicentral distance from hypocenters of Cushing earthquake sequence. Two close stations OK052 and OK053 were available several days after the mainshock. Grey lines

show mapped faults from OGS database (Marsh and Holland, 2016). Red, blue and green circles denote 3, 6, and 10 miles radius, respectively. (b) A zoomed-in plot of the study region. Size of red squares (wells) is scaled with the total water injection volume from 2014 to 2018, in million barrels. Colored stars and circles show relocated M>4 earthquakes and their aftershocks (within 20 days). Focal mechanisms are displayed as colored beach balls (parameters in Table 1). (c) A depth section of events along the AA' profile in (b). Four aftershocks denoted with white pluses are used as reference events for velocity structure calibration. (d) A depth section of events along the BB' profile in (b).

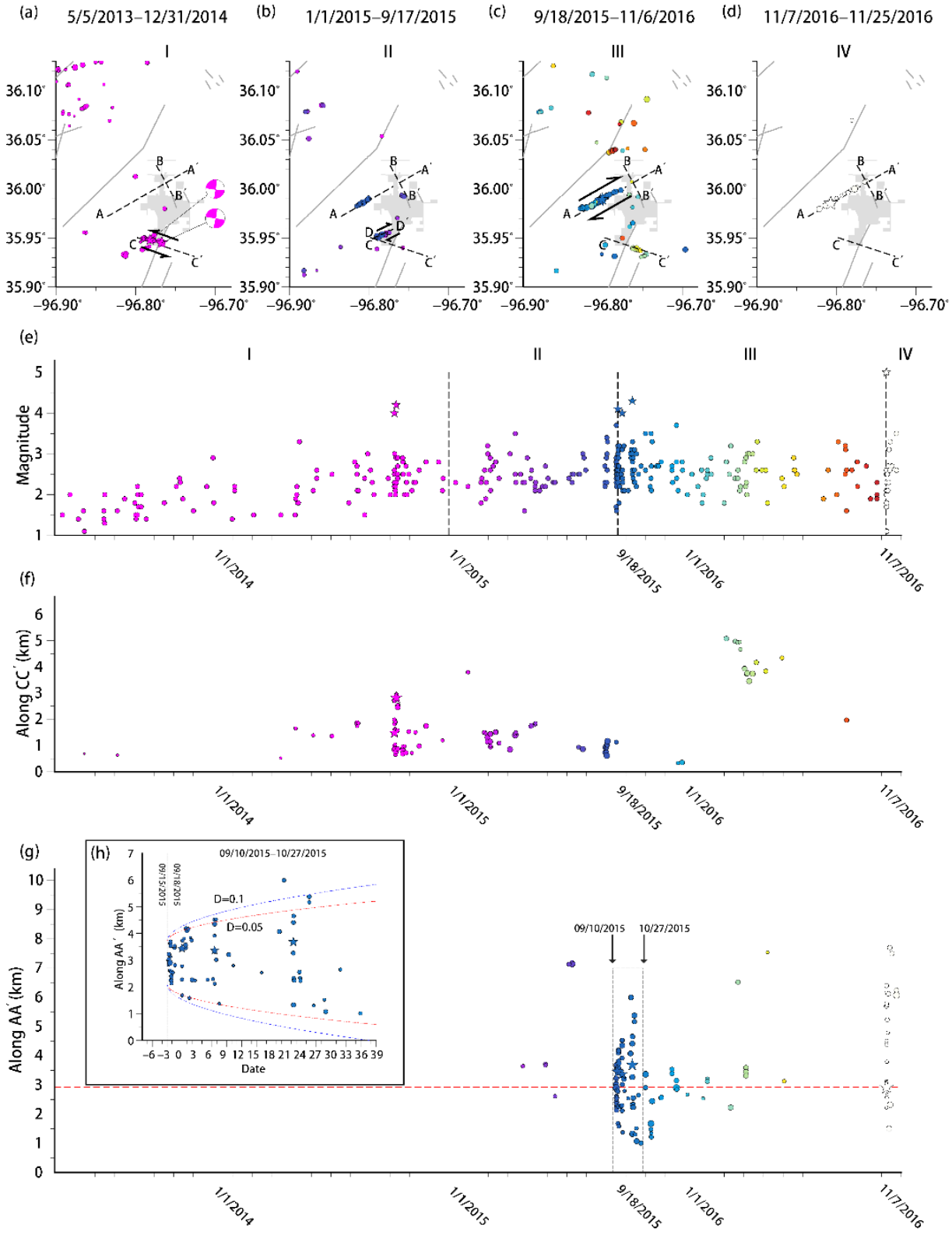
(a) 5/5/2013–12/31/2014
(b) 1/1/2015–9/17/2015
(c) 9/18/2015–11/6/2016
(d) 11/7/2016–11/25/2016
I
II
III
IV
36.10°
36.05°
36.00°
35.95°
35.90°
−96.90°
−96.80°
−96.70°
A
A′
B
B′
C
C′
D
(e)
Magnitude
1/1/2014
1/1/2015
9/18/2015
1/1/2016
11/7/2016
(f)
Along CC′ (km)
(g)
Along AA′ (km)
09/10/2015
10/27/2015
(h)
09/10/2015–10/27/2015
09/18/2015
09/15/2015
D=0.1
D=0.05
Along AA′ (km)
Date

563

Figure 2. Geographic distribution of seismicity (Schoenball and Ellsworth 2017a) for different time stages (a) I: May 2013 to Dec. 31, 2014. The beachballs represent the focal mechanisms of two M4 earthquakes happened in 2014 on south of Cushing fault AA'. (b) II: Jan.1, 2015 to Sep.17, 2015 (c) III: Sep.18, 2015 to Nov. 6, 2016 (d) IV: Nov.7, 2016 to Dec.25, 2016. Faults AA' and DD' are in right-lateral motions and fault CC' is in left-lateral motion. (e) Magnitude-Time plot of seismicity during different time stages. (f) Evolution of the earthquake locations along fault CC' vs time. (g) Evolution of earthquake locations along fault AA' vs time. The horizontal red dashed line denotes the location of the M 5 mainshock hypocenter. (h) A zoomed-in plot showing earthquake evolution within the dashed box in (g). Two colored dashed lines show the fluid diffusion curves with diffusivity D=0.05 (red) and D=0.1 (blue).

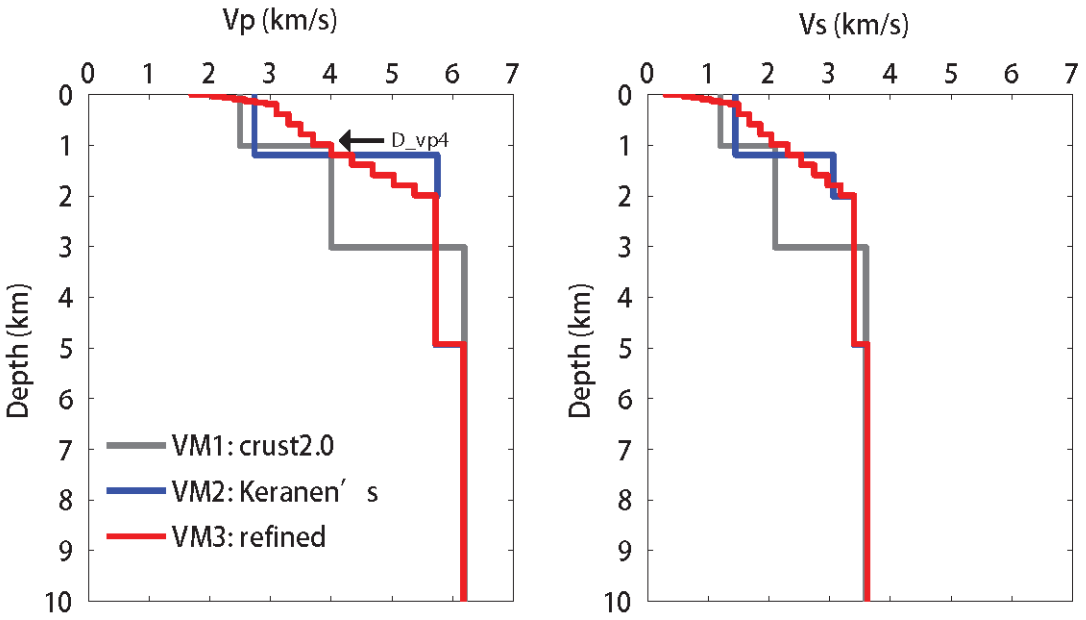

575

576Figure 3. Vp and Vs velocity models used in this study (Gray, VM1: Crust2.0 models; Blue, VM2: Karanen

577et al. (2013); Red, VM3: a refined version of Keranen's model). D_vp4 is the grid searched depth of

578Vp=4km/s.

579

61

62

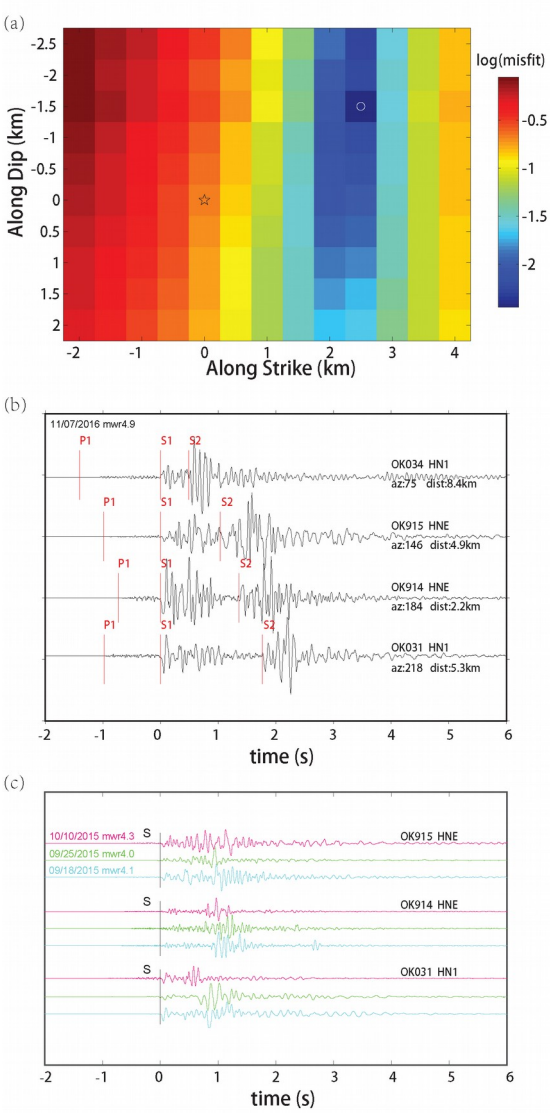

Figure 4. Modeling of the two sub-events of the M5 earthquake. (a) Location of the second sub-event from fitting the differential S-wave arrival time of two sub-events. The black star is the hypocenter the first sub-event and the white circle is the preferred location of the second sub-event. (b) Raw seismic waveforms for the M5 mainshock on four stations. The P wave and S wave arrivals for the first sub-event are labeled as P1 and S1. And S arrival for the second sub-event is labeled as S2, with S1 aligned at 0 s. (c) Raw seismic waveforms for three M4+ earthquakes on three stations, with S arrival time aligned at 0 s.

588

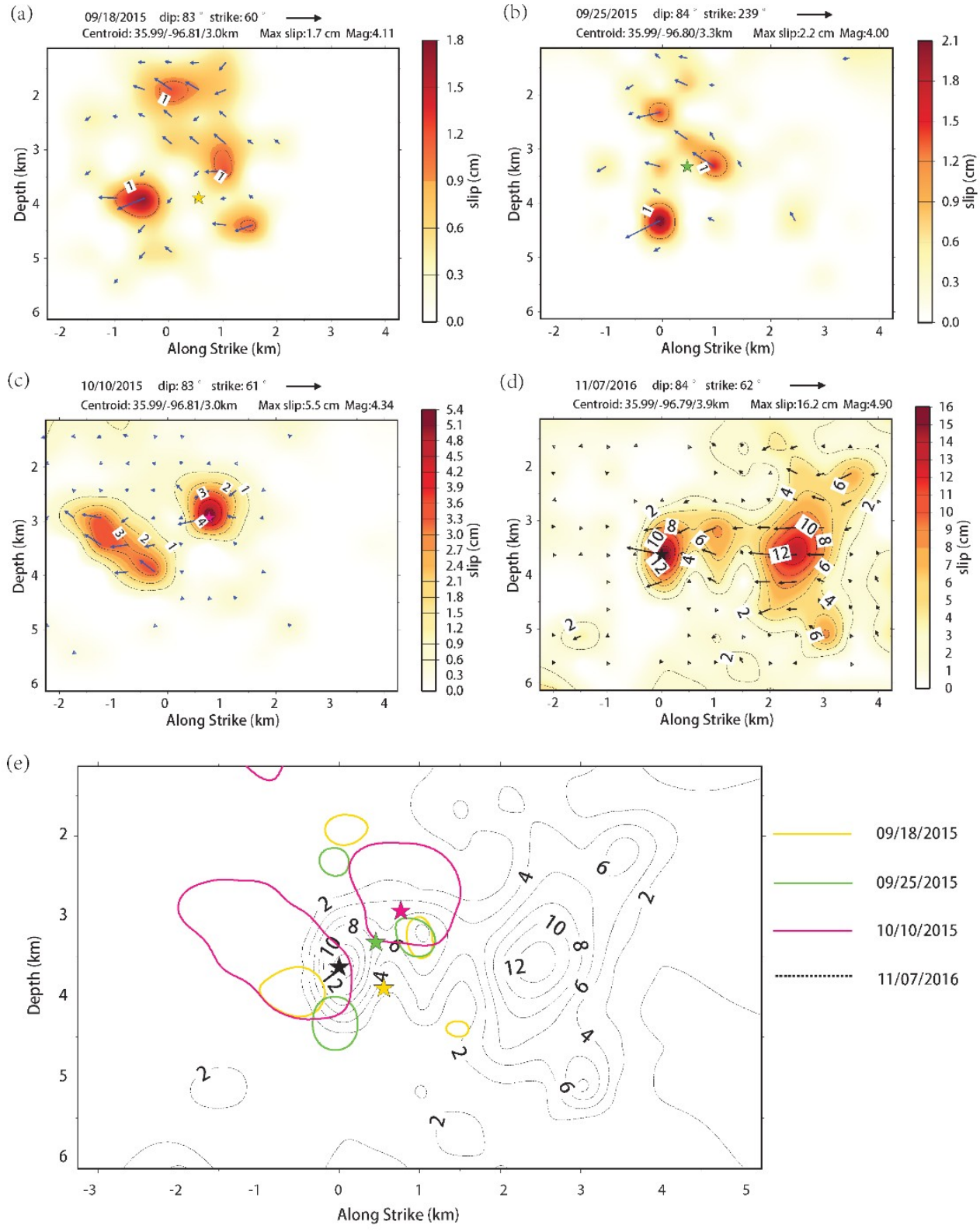
(a)
09/18/2015 dip: 83 ° strike: 60 °
Centroid: 35.99/-96.81/3.0km Max slip:1.7 cm Mag:4.11
(b)
09/25/2015 dip: 84 ° strike: 239 °
Centroid: 35.99/-96.80/3.3km Max slip:2.2 cm Mag:4.00
(c)
10/10/2015 dip: 83 ° strike: 61 °
Centroid: 35.99/-96.81/3.0km Max slip:5.5 cm Mag:4.34
(d)
11/07/2016 dip: 84 ° strike: 62 °
Centroid: 35.99/-96.79/3.9km Max slip:16.2 cm Mag:4.90
(e)
Depth (km)
Along Strike (km)
slip (cm)
09/18/2015
09/25/2015
10/10/2015
11/07/2016

589

65

66

Figure 5. Rupture models from finite fault inversion of (a) the 09/18/2015 *Mw* 4.1, (b) the 09/25/2015 *Mw* 4.0, (c) the 10/10/2015 *Mw* 4.3, and (d) the 11/07/2016 *Mw* 4.9 earthquake. The colored stars denote the hypocenters of four target earthquakes. The blue arrows in each panel represents the inverted slip direction and magnitude at each cell. The centroid location, the maximum slip and magnitude, and fault geometry information (dip and strike angles) are shown on the top of each panel. (e) The 1 cm slip contours for three 2015 M 4+ events, and the full slip contour for the 2016 mainshock.

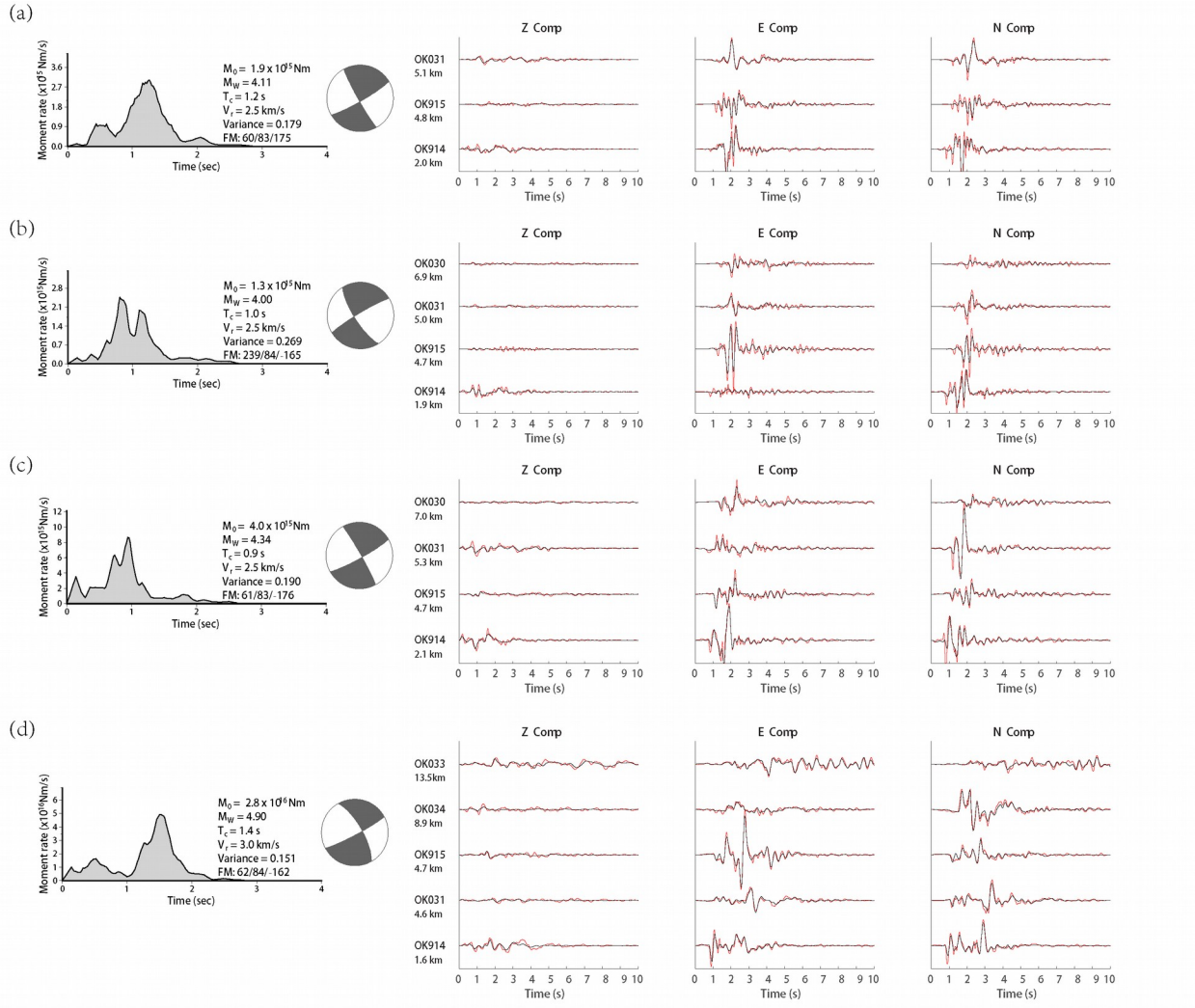

598

599Figure 6. Source time function and seismic waveform fitting on nearby stations for (a) the 09/18/2015

600event (b) the 09/25/2015 event (c) the 10/10/2015 event (d) the 11/07/2016 mainshock. The vertical (Z),

601east (E) and north(N) components are displayed from left to right. Station code and epicentral distance

602are also labeled.

603

604

605

69

70

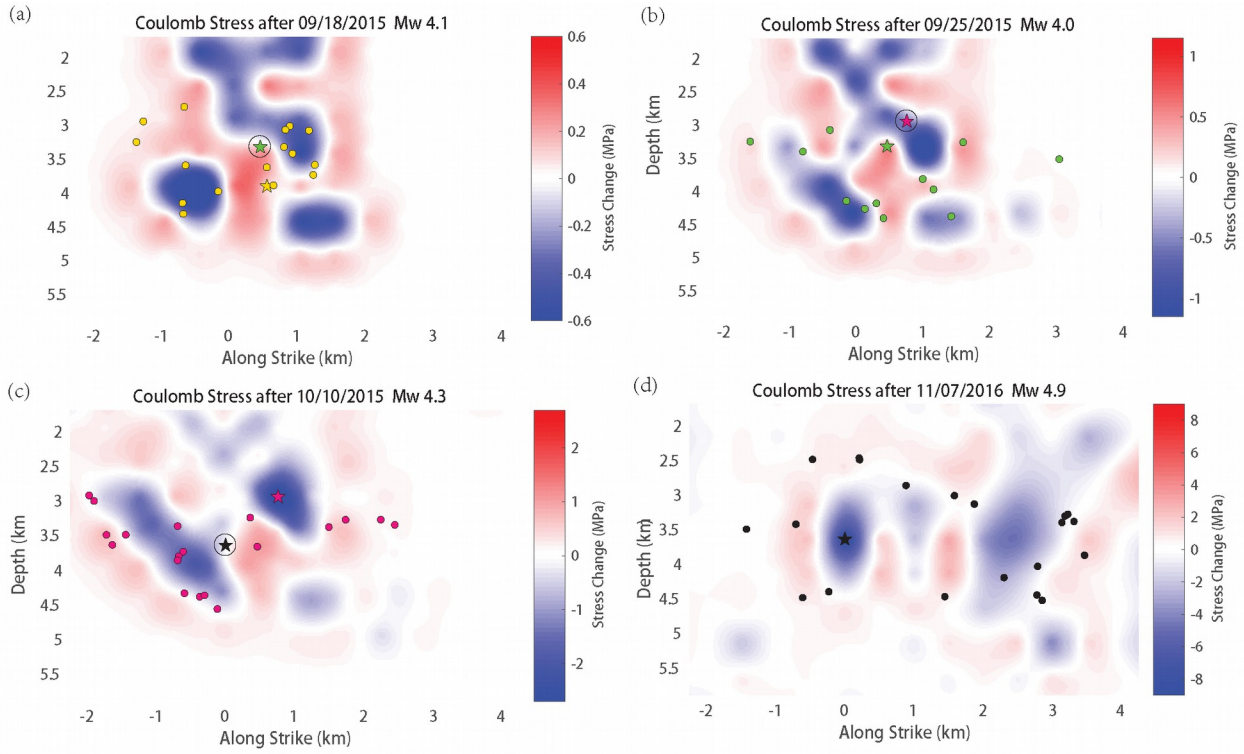

606

607Figure 7. (a) Cumulative Coulomb stress change on the causative fault, immediately after the
60809/18/2015 Mw 4.1 event, based on the finite fault model in Figure 3. The yellow star and dots
609are locations of the hypocenter and aftershocks of the 09/18/2015 event, while the circled green
610star represents hypocenter of the 09/25/2015 Mw 4.0 event. (b) Cumulative Coulomb stress
611change after adding the Coulomb stress change from the 09/18/2015 and 09/25/2015 events. The
612green star and dots are locations of hypocenter and aftershocks of the 09/25/2015 event, while
613the circled magenta star represents hypocenter of the 10/10/2015 Mw 4.3 event. (c) Cumulative
614Coulomb stress change after adding the Coulomb stress change from the 09/18/2015, 09/25/2015
615and 10/10/2015 events. The magenta star and dots are locations of hypocenter and aftershocks of
616the 10/10/2015 event, while the circled black star represents hypocenter location of the
61711/07/2016 M 5 event. (d) Cumulative Coulomb stress change after summing from the four M4+

71

72

earthquakes in the Cushing sequence. The black star and dots are locations of hypocenter and aftershocks of the 11/07/2016 event.

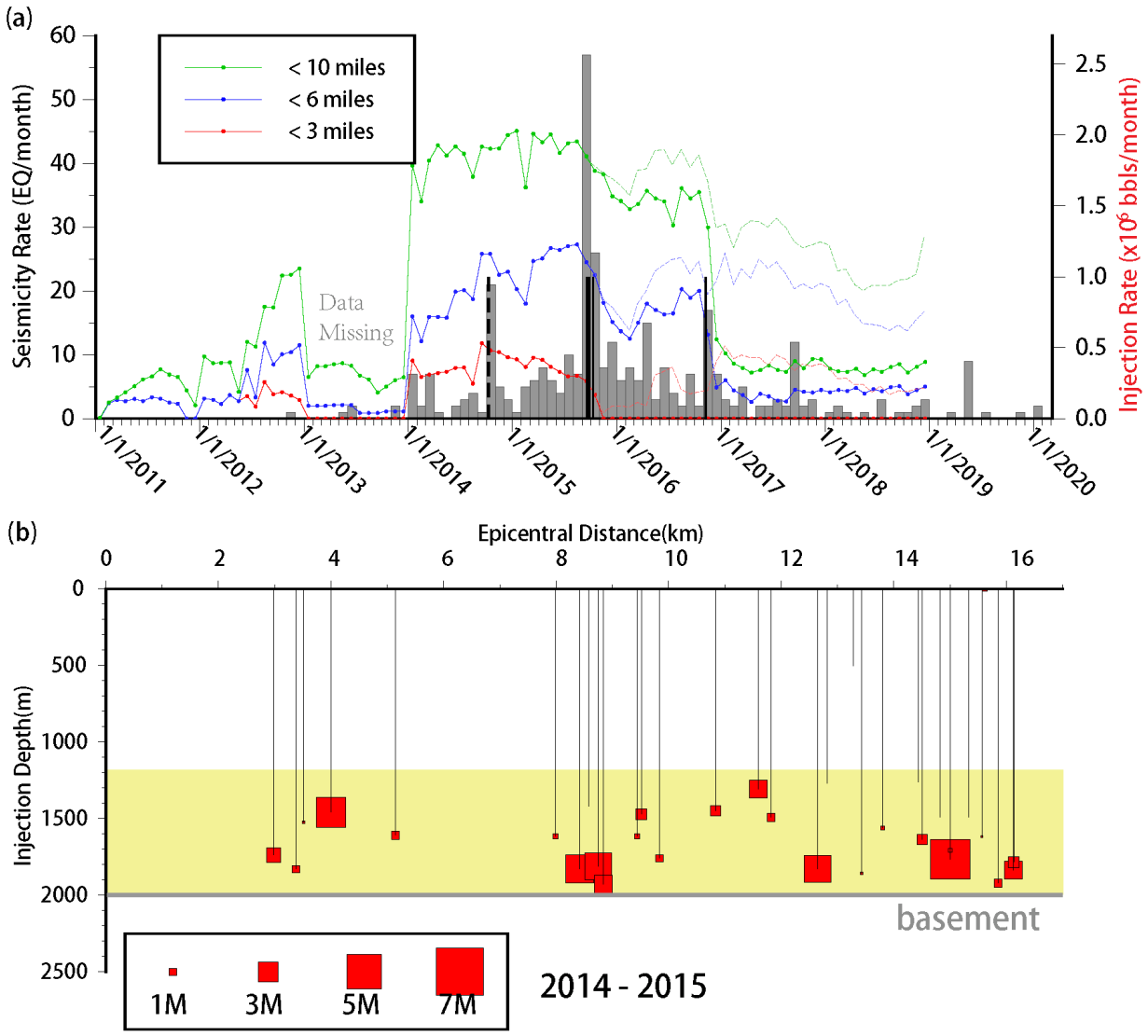

621

622Figure 8. Water injection history in disposal wells near Cushing city and evolution of seismicity.
623(a) Monthly water injection volume, from Jan. 2011 to Dec. 2018, of disposal wells within 3
624miles (red line),6 miles (blue line) and 10 miles (green line) from the 11/07/2016 mainshock
625epicenter. The dashed lines represent the total monthly injection volume into the crust after
626September 2015 and the solid lines represent volume injected into the Arbuckle group. Grey
627bars are numbers of earthquakes in each month which occurred within 10 miles from the
628mainshock epicenter, shown in Fig. 1a. Black vertical lines denote the four M >4 earthquakes in

2015-2016 and the dashed vertical line denote two M>4 earthquakes happened in Oct. 2014 to the south of the Cushing fault. The water injection data were not available from 2013 to 2014 near Cushing area. (b) Well completion depths and injection volume in 2014 and 2015, of each disposal wells within 10 miles from the M5 mainshock hypocenter. The red squares show depth of the wells with size of the squares denoting total water injection volume at each well.

635

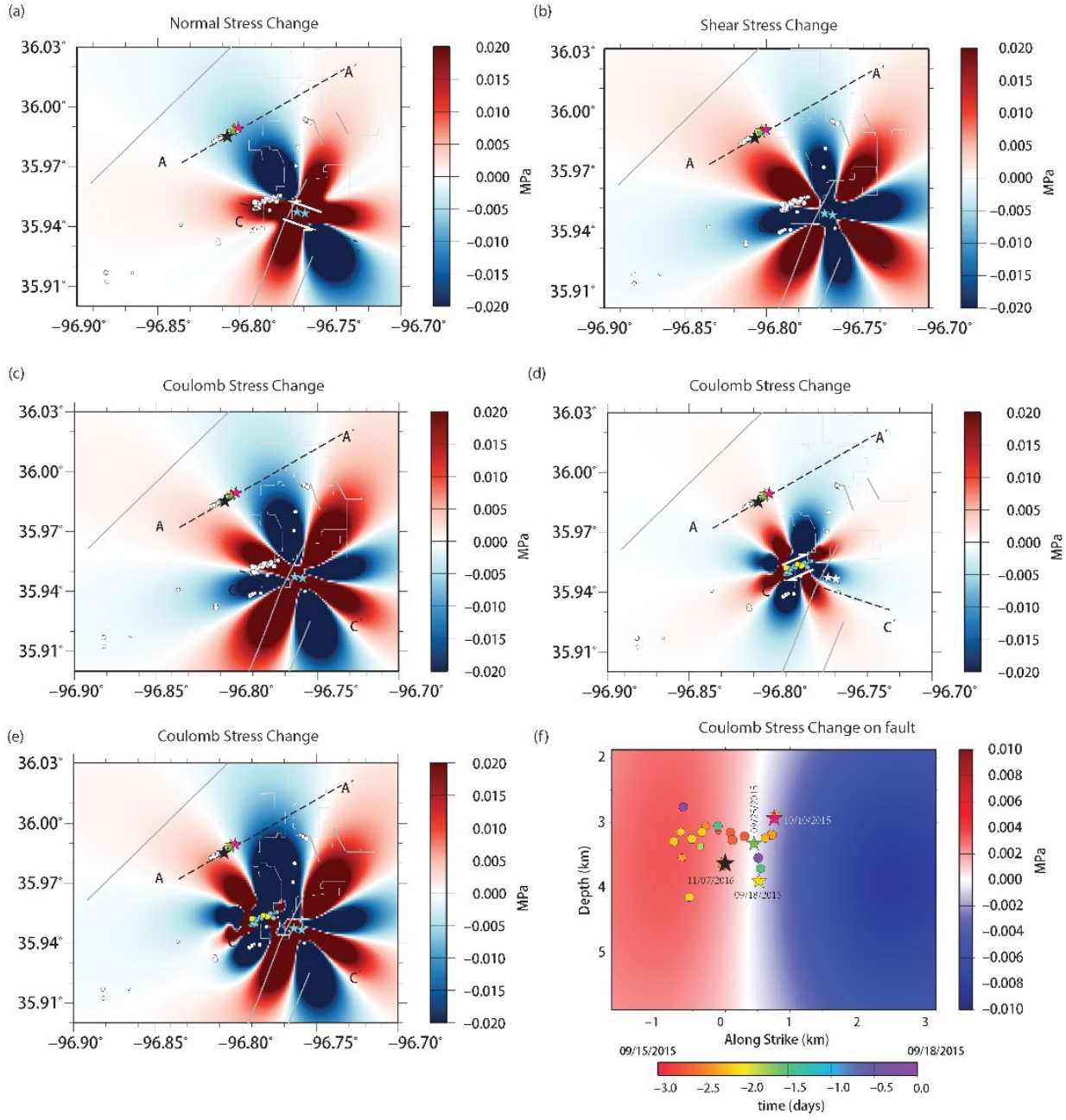

636

637Figure 9. Coulomb stress changes resolved on right-lateral fault, striking 60 degrees with
638effective friction coefficient on fault set as 0.4. (a) Normal stress change at depth of 3km, caused
639by two M4 left-lateral earthquakes (cyan stars) occurred in October 2014 south of Cushing city.
640The focal mechanisms and centroid locations of these two M4 earthquakes are from McNamara

et al. (2015). The color saturation is set at a small value of 0.2 MPa, to better show small Coulomb stress change for a larger area. Negative values mean clamping on the fault. (b) Shear stress change at depth of 3 km, caused by two M4 left-lateral earthquakes occurred in October 2014 on the south of Cushing city. (c) Coulomb stress change at depth of 3 km, caused by two M4 left-lateral earthquakes occurred in October 2014 south of Cushing city. (d) Coulomb stress change at depth of 3 km, caused by many right-lateral strike-slip earthquakes (cyan circles) occurred after two left-lateral M4 earthquakes in 2014 and before the Mw 4.1 09/18/2015 earthquake. The yellow circles are M>3 earthquakes shown in Figure S3. (e) Coulomb stress change at depth of 3 km, contributed from the left-lateral and right-lateral earthquakes shown in (c) and (d). (f) Coulomb stress change on the cross section along the AA' Cushing fault, caused by summing contributions from both left-lateral and right-lateral earthquakes. The colored circles are foreshocks occurred within three days before the 09/18/2015 Mw 4.1 event, with color of circles representing their relative occurrence times. The locations of Cushing earthquake sequence in this study are marked by colored stars and labelled by time.

Table 1. Fault plane solutions of the four earthquakes from waveform inversion with the Cut and Paste (CAP) method

Date (mm/dd/yyyy)	Magnitude (*Mw*)	Centroid Depth (km)	Nodal Plane 1 Strike(°)/Dip(°)/Rake(°)	Nodal Plane 2 Strike(°)/Dip(°)/Rake(°)
09/18/2015	4.08	4.0	60/83/175	151/86/7
09/25/2015	3.95	3.3	249/84/-165	148/76/-6
10/10/2015	4.32	3.6	61/83/-176	331/87/-7
11/07/2016	4.89	4.7	61/84/-162	330/73/-6